Deutsches Elektronen-Synchrotron DESY

H1prelim-22-034, contributed to the DIS2022 conference
April 26, 2022

Multi-differential Jet Substructure Measurement in High Q^2 DIS Events with HERA-II Data

H1 Collaboration

Abstract

A measurement of different jet substructure observables in high Q^2 neutral-current deep-inelastic scattering events close to the Born kinematics is presented. Differential and multi-differential cross-sections are presented as a function of the jet's charged constituent multiplicity, momentum dispersion, jet charge, as well as three values of jet angularities. Results are split into multiple Q^2 intervals, probing the evolution of jet observables with energy scale. These measurements probe the description of parton showers and provide insight into non-perturbative QCD. Unfolded results are derived without binning using the machine learning-based method Omnifold. All observables are unfolded simultaneously by using reconstructed particles inside jets as inputs to a graph neural network. Results are compared with a variety of predictions

Short-distance interactions between quarks and gluons (partons) are described by the theory of Quantum Chromodynamics (QCD). At high energy particle colliders, outgoing partons manifest as collimated sprays of particles known as jets. The radiation pattern inside jets (jet substructure) provides insight into the emergent properties of QCD at high energies. Previous studies at the HERA experiment on jet observables in deep inelastic scattering (DIS) at high photon virtuality (Q^2) were performed by the ZEUS [1–3] and H1 [4] Collaborations. After the end of the data-taking period of the HERA experiment, new studies on jet physics were proposed to disentangle quark and gluon jets [5,6] and to validate parton shower models [7] using jet substructure observables as probes. In particular, a generalized set of jet angularities λ_β^κ were proposed in [5] defined as:

$$\lambda_\beta^\kappa = \sum_{i \in \text{jet}} z_i^\kappa \left(\frac{R_i}{R_0}\right)^\beta, \tag{1}$$

with z_i representing the ratio $p_{T,i}/p_{\text{T}}^{\text{jet}}$ for a particle with transverse momentum $p_{T,i}$ clustered inside a jet with distance parameter R_0 and momentum $p_{\text{T}}^{\text{jet}}$. The parameter R_i describes the distance between the particle and the jet axis defined as $R_i = \sqrt{(\eta_i - \eta^{\text{jet}})^2 + (\phi_i - \phi^{\text{jet}})^2}$.

Furthermore, this set of observables can be extended by including the electric charge information from the hadrons clustered inside the jet. The charged particle multiplicity N_c is identified as λ_0^0 with summation in Eq. 1 performed over only charged particles, while the jet charge Q_κ is identified as $\tilde{\lambda}_0^\kappa$ after including the weighted charge sum as:

$$\tilde{\lambda}_0^\kappa = Q_\kappa = \sum_{i \in \text{jet}} q_i \times z_i^\kappa. \tag{2}$$

In this work, multi-differential cross sections as a function of six jet observables are measured in neutral current DIS events at the Born level limit using the data recorded by the H1 detector. Those include three infrared and collinear (IRC) unsafe distributions: the momentum dispersion $p_{\text{T}}\text{D}^2 = \lambda_0^2$ [8–10], $N_c = \lambda_0^0$, and jet charge $Q_1 = \tilde{\lambda}_0^\kappa$ [7, 11] as well as three IRC safe observables: the jet thrust (λ_2^1) [12], jet broadening (λ_1^1) [13–15], and an intermediate value $\lambda_{1.5}^1$. The different observables measured in this work are represented in Fig. 1.

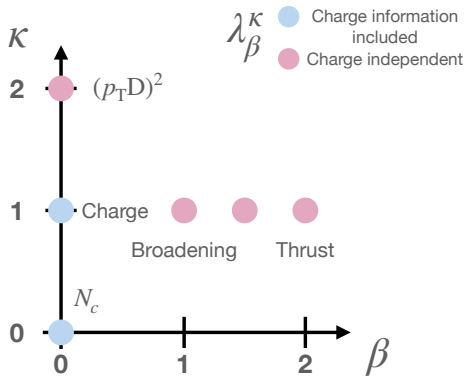

Fig. 1: Visualization of the jet observables measured in this work. Jet angularities are calculated using all particles clustered in the same jet while charged particle multiplicity N_c and jet charge Q_1 consider only the charged particles inside the jet and the charge weighted sum in Eq. 1, respectively.

Normalized multi-differential results are reported as a function of the scale Q^2 , probing the jet substructure evolution as a function of the energy scale and providing complementary information to planned studies on jet substructure at the EIC [16, 17] that covers the low Q^2 regime. New machine learning

methods are used to simultaneously unfold all measured quantities to generator level, leveraging advancements in graph neural networks for collider physics and incorporating more information to the unfolding procedure.

1 Experimental method

The full description of the H1 detector can be found elsewhere [18–22] while main detector components that are most relevant for this measurement are described below. Results are reported using the right handed coordinate system with positive z direction pointing on the direction of the proton beam with interaction point located at $z = 0$. The polar angle θ, is defined with respect to this axis. The pseudorapidity is defined as $\eta_{\text{lab}} = -\ln\tan(\theta/2)$. The main sub-detectors used in this analysis are the inner tracking detectors and the Liquid Argon (LAr) calorimeter, which are both immersed in a magnetic field of 1.16 T provided by a superconducting solenoid. The central tracking system, which covers $15^\circ < \theta < 165^\circ$ and the full azimuthal angle, consists of drift and proportional chambers that are complemented with a silicon vertex detector in the range $30^\circ < \theta < 150^\circ$ [23]. It yields a transverse momentum resolution for charged particles of $\sigma_{p_T}/p_T = 0.2\%\ p_T/\text{GeV} \oplus 1.5\%$. The LAr calorimeter, which covers $4^\circ < \theta < 154^\circ$ and full azimuthal angle, consists of an electromagnetic section made of lead absorbers and a hadronic section with steel absorbers; both are highly segmented in the transverse and longitudinal directions. Its energy resolution is $\sigma_E/E = 11\%/\sqrt{E/\text{GeV}} \oplus 1\%$ for leptons [24] and $\sigma_E/E \approx 50\%/\sqrt{E/\text{GeV}} \oplus 3\%$ for charged pions [25]. In the backward region ($153^\circ < \theta < 177.5^\circ$), energies are measured with a lead-scintillating fiber calorimeter [22]. Results are reported using the data recorded by the H1 detector in the years 2006 and 2007 when electrons [1] and protons were collided at energies of 27.6 GeV and 920 GeV, respectively. The total integrated luminosity of this data sample corresponds to 228 pb^{-1} [26].

Events are triggered by requiring a high energy cluster in the electromagnetic part of the LAr calorimeter. The scattered electron is identified as the highest transverse momentum LAr cluster matched to a track that passing an isolation criteria [27]. Events containing scattered electrons with energy $E_{e'} > 11$ GeV are kept for further analysis, resulting in a trigger efficiency higher than 99.5% [28, 29]. Backgrounds from additional processes such as cosmic rays, beam-gas interactions, photoproduction, charged-current DIS and Quantum Electrodynamics (QED) Compton processes are rejected after dedicated selection [29, 30], resulting in negligible background contamination.

Relevant DIS variables are reconstructed using the Σ method [31] defined as:

$$y = \frac{\sum_{i\in\text{had}}(E_i - p_{i,z})}{\sum_{i\in\text{had}}(E_i - p_{i,z}) + E_{e'}(1-\cos\theta_{e'})}$$
$$Q^2 = \frac{E_{e'}^2 \sin^2\theta_{e'}}{1-y}$$

where $\theta_{e'}$ is the polar angle of the scattered electron and $\sum(E_i - p_{i,z})$ is the total difference between the energy and longitudinal momentum of the entire hadronic final state (HFS). HFS objects are reconstructed using the energy flow algorithm [32–34] after removing energy clusters and tracks associated to the electron. Additionally, events are required to have $45 < \sum(E_i - p_{i,z}) < 65$ GeV to suppress initial-state QED radiation.

Jets are defined in the laboratory frame by clustering HFS objects satisfying $-1.5 < \eta_{\text{lab}} < 2.75$. The FastJet 3.3.2 package [35, 36] is used with k_T clustering algorithm [37, 38] with distance parameter $R = 1$. Events containing at least one jet with $p_T > 5$ GeV are kept for further analysis.

Generator level ("particle level") observables are calculated in the simulation using final-state particles with proper lifetime $c\tau > 10$ mm and excluding the scattered lepton. Reconstructed and generator level

[1] In this document, the term 'electron' is used generically to refer to both electrons and positrons

jets are matched by requiring the distance $\Delta R = \sqrt{(\phi^{\text{jet}}_{\text{gen}} - \phi^{\text{jet}}_{\text{reco}})^2 + (\eta^{\text{jet}}_{\text{gen}} - \eta^{\text{jet}}_{\text{reco}})^2} < 0.9$.

Results are presented after unfolding the data to generator level for events in the kinematic region defined by $Q^2 > 150$ GeV^2 , $0.2 < y < 0.7$, $p^{\text{jet}}_{\text{T}} > 10$ GeV, and $-1.0 < \eta^{\text{jet}}_{\text{lab}} < 2.5$.

2 Monte Carlo simulations

Monte Carlo (MC) simulations are used to correct the data for detector acceptance and resolution effects as well as to compare theoretical predictions with unfolded results.

Detector acceptance and resolution effects are estimated using DJANGOH [39] 1.4 and RAPGAP [40] 3.1 simulators. Both generators implement Born level matrix elements for neutral current DIS, boson–gluon fusion, and QCD Compton processes and are interfaced with HERACLES [41–43] for QED radiation. The CTEQ6L PDF set [44] and the Lund hadronization model [45] with parameters determined by the ALEPH Collaboration [46] are used for the non-perturbative components. DJANGOH uses the Colour Dipole Model as implemented in ARIADNE [47] for higher order emissions, and RAPGAP uses parton showers in the leading logarithmic approximation. Each of these generators is combined with a detailed simulation of the H1 detector response based on the GEANT3 simulation program [48] and reconstructed in the same way as data.

Predictions from PYTHIA 8.3 [49, 50] are used for comparison using the default implementation and two additional parton shower implementations: VINCIA [51, 52] and DIRE [53]. VINCIA uses a p_{T}-ordered model for QCD + QED showers based on the antenna formalism while DIRE implements a p_{T} ordered dipole shower similar to ARIADNE. The NNPDF3.1 PDF set [54] is used for both default and VINCIA implementation and MMHT14nlo68cl PDF set [55] is used for the DIRE implementation. Predictions from HERWIG 7.2 [56, 57] are calculated using the default implementation parameters and the CT14 [58] PDF set.

3 Unfolding methodology using a graph neural network together with Omnifold

The unfolding procedure is carried out by simultaneously unfolding all jet observables and Q^2 distribution at the same time using the OMNIFOLD method [59, 60] in an unbinned manner. OMNIFOLD corrects the data for detector effects using machine learning in a iterative reweighting process that is unbinned and naturally incorporates high dimensional inputs. This method is also a generalization of the iterative unfolding approach [61–63] used for binned distributions.

At each iteration, OMNIFOLD defines a set of classifiers to estimate likelihood ratios that are used as event weights. In each iteration, a two-step approach is used, defining two independent classifiers. In the first step, a classifier is trained to distinguish data from simulated events while the second step updates the simulation by training a classifier to distinguish between the original simulation and the simulation weighted after the first step. This second step only uses the generator level information of simulated events as inputs, producing a weight map that is a proper function of the particle level inputs. The updated simulation is then used as the starting point for the following OMNIFOLD iteration. This process is repeated a total of six times in this work. The number of iterations is chosen as the one yielding the lowest overall systematic uncertainty of the unfolded results reported.

All jets observables used in this document are calculated based on HFS objects clustered inside the jets. Instead of using only the jet observables as inputs to the machine learning classifiers, a hybrid approach was used. In the first step, the inputs used are directly the HFS objects reconstructed in data and simulation. For each HFS object with momentum (p_{T},η,ϕ) and electric charge c, the kinematic information used for the classifier training is the set (z,$\Delta\eta$,$\Delta\phi$,c), with $z = p_{\text{T}}/p^{jet}_{\text{T}}$, $\Delta\eta = \eta - \eta^{jet}$, and $\Delta\phi = \phi - \phi^{jet}$. Jet momentum ($p^{jet}_{\text{T}}$, η^{jet},ϕ^{jet}) and Q^2 information is also included as inputs. Leveraging

the success of Graph Neural Networks (GNNs) for jet classification [64–75] based on particle sets as inputs, the PCT [72] GNN architecture is chosen to train the classifier during the first step. The local neighborhood in PCT is defined by selecting the five closest neighbors of each particle with distances calculated in the $\eta - \phi$ space. Up to 30 HFS objects, ordered by transverse momentum, are considered per jet during training. Inputs are truncated in case more particles are present and zero-padded otherwise. All measured quantities were verified to not be affected after truncating the total number of particles considered.

In the second step, a simplified classifier architecture is used. The inputs of the classifier are the same jet kinematic information and Q^2 used in the previous step, but HFS objects are replaced by the jet observables that are reported in the final results. This choice decreases the number of inputs by an order of magnitude and reduce the training time of the classifier by a factor 5. Since the first step is tasked to incorporate as much information as possible from the data, the simplified classifier adopted for the second step does not degrade the unfolding results while greatly reducing the computational cost of the method. This simplified classifier is implemented using a dense neural network with three hidden layers with 68, 128, and 68 nodes per layer.

The output of all classifiers are passed through a sigmoid activation function and trained using the binary cross-entropy loss function. The training proceeds until the validation loss, estimated with an independent data set, does not improve for 10 consecutive epochs. All machine learning methods are implemented in KERAS [76] and TENSORFLOW [77] using the ADAM [78] optimization algorithm. The full unfolding process is carried out using 128 graphic processing units (GPUs) simultaneously with the Perlmutter [79] supercomputer and HOROVOD [80] library used for distributed training.

4 Uncertainties

Systematic uncertainties on the detector description are estimated by varying the relevant aspect of the simulation and carrying out the full unfolding procedure with the varied simulation set. Uncertainties on HFS objects include the energy scale from two different contributions: HFS objects contained in high p_{T} jets and other HFS objects. In both cases, the energy-scale uncertainty is $\pm 1\%$. Both uncertainty sources are estimated separately [81, 82] by varying the corresponding HFS energy by $\pm 1\%$. An uncertainty of ± 20 mrad is assigned to the azimuthal angle determination of HFS objects. Lepton uncertainties are considered in the Q^2 determination and the uncertainty on the lepton energy scale ranges from $\pm 0.5\%$ to $\pm 1\%$ [82, 83]. Uncertainties on the azimuthal angle of the scattered lepton are estimated to be ± 1 mrad [84]. Additional uncertainties from the unfolding procedure are estimated to cover a possible bias from the generator choice used to perform the unfolding procedure. Those include a model uncertainty, estimated by the difference in results obtained when performing the unfolding with the RAPGAP or DJANGOH simulations, and a non-closure uncertainty, estimated by the difference between the DJANGOH simulation at generator level and the unfolded results from RAPGAP unfolded to the DJANGOH simulation. QED corrections accounting for virtual and real higher-order QED effects are taken as an uncertainty and are estimated by comparing the simulation response with and without initial QED radiation with residual differences taken as the uncertainty. The statistical uncertainty is estimated using the bootstrap technique [85]. The unfolding procedure is repeated on 100 pseudo datasets, each defined by resampling the original dataset with replacement. Normalization uncertainties, such as luminosity scale and trigger efficiencies, cancel in the ratio of the normalized differential cross section results.

5 Results

Unfolded results are presented in Fig. 2 for events with $Q^2 > 150$ GeV^2 and $0.2 < y < 0.7$, while Fig. 3 shows the evolution of each observables in different Q^2 intervals. The comparison with theory predictions are split into DIS dedicated predictions (RAPGAP and DJANGOH) and general purpose simulators

(PYTHIA and HERWIG). Predictions from RAPGAP and DJANGOH, show an overall good description of the data. In particular, the RAPGAP simulation remarkably agrees with data for all distributions in all Q^2 intervals within uncertainties. The jet charge distribution is better described by the DJANGOH simulation while the PYTHIA implementation with VINCIA parton showering agrees with data for $Q^2 > 360$ GeV^2 and shows a disagreement at the tails of the distribution at low Q^2 intervals. All predictions are also able to capture correctly the mean value of the jet charge. Charged particle multiplicity shows a large disagreement for all general purpose simulations at low Q^2 values with average number of charged particles underestimated by all PYTHIA implementations and overestimated for HERWIG. This disagreement however is mitigated as Q^2 increases. The momentum dispersion is well described by the dedicated DIS simulators, PYTHIA + DIRE, and HERWIG predictions. The agreement is also improved for all predictions with increasing values of Q^2 . In all IRC safe jet angularities, the data is well represented by the RAPGAP and HERWIG simulations in all Q^2 intervals. Predictions from PYTHIA + DIRE show the best agreement of the alternative parton shower implementations used. The agreement with data is also improved at higher Q^2 values for all PYTHIA predictions, while the DJANGOH simulation shows a better data description at lower Q^2 intervals.

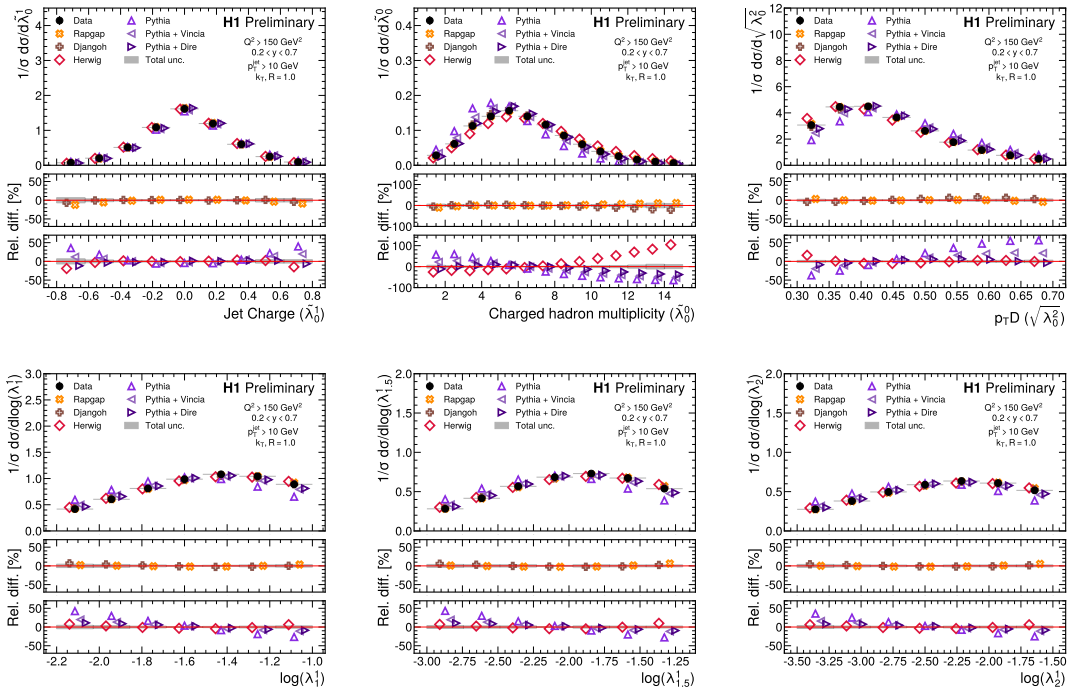

Fig. 2: Measured cross sections, normalized to the inclusive jet production cross section as a function of the jet observables reported in this work. Predictions from multiple simulations are shown for comparison. The percent difference between data and predictions is shown in the bottom panels, split into dedicated DIS simulators (middle) and general purpose simulators (bottom). Gray bands represent the total systematic uncertainty. Statistical uncertainties for data events are shown as vertical bars, while statistical uncertainties from simulations are smaller than the marker size.

6 Conclusion

A measurement of jet substructure observables in neutral current DIS events with $Q^2 > 150$ GeV^2 and $0.2 < y < 0.7$ as well as divided in four Q^2 intervals is presented. These measurements include a combination of IRC safe and unsafe distributions described by a set of generalized jet angularities. These distributions are sensitive to perturbative QCD effects and to hadronization models used to describe jet formation. Theory predictions from dedicated DIS simulators show an overall good description of all

measured quantities. In particular, a good agreement between data and RAPGAP simulation is observed for all distributions and Q^2 intervals. General purpose simulators are also able to describe well the data. In particular, HERWIG predictions show a good agreement in all IRC safe observables. The nominal PYTHIA predictions show large disagreements with data, while alternative parton showers were found to improve the data agreement in all measured observables compared to the default parton shower implementation.

Unfolded results to generator level are reported using novel machine learning methods. All measured distributions are simultaneously unfolded using the OMNIFOLD method. Kinematic information from each particle clustered inside a jet is extracted by means of a dedicated graph neural network implementation named PCT. The training of the method is carried out using the Perlmutter supercomputer with 128 GPUs used simultaneously during unfolding.

Results provided in this work represent the first time a set of jet angularities has been measured in electron-proton collisions and serve as a complementary guide to jet substructure studies at the future Electron-ion Collider.

Results presented in this work represent the first step in the direction of unfolding any jet substructure observable calculated with the set of particles used during the jet clustering step. This opens the possibility of including the unfolding information during the experimental design as opposed to the last step of the measurement, leading to better optimization routines based on unfolded distributions.

Acknowledgements

Appendices

A Data and simulation comparison at reconstruction level

Prior to unfolding, a comparison between the data and simulation is performed using the selection criteria described in Sec. 1. Both RAPGAP and DJANGOH simulations are used in the comparisons shown in Figs. 4 and Fig. 5.

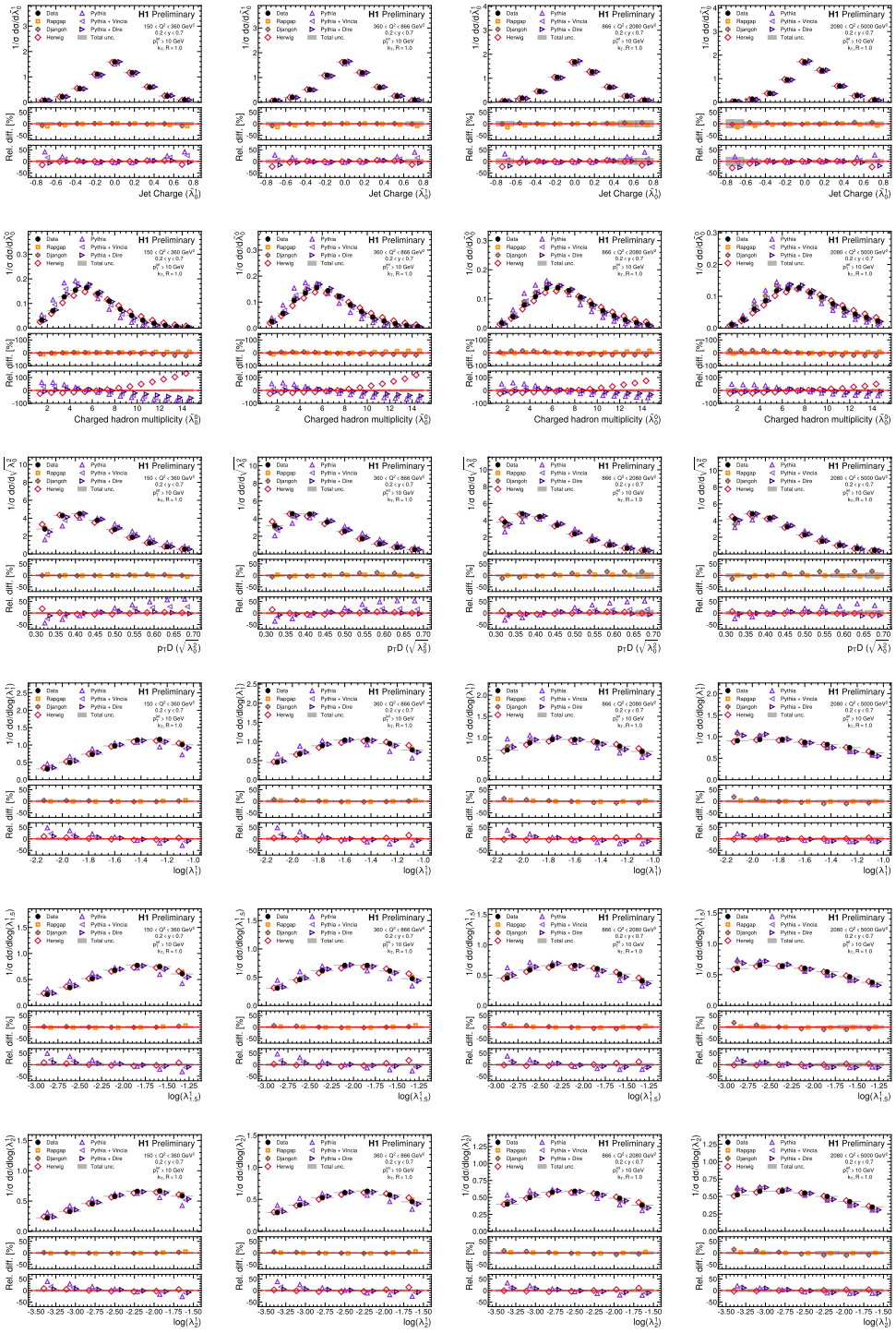

Fig. 3: Measured cross sections, normalized to the inclusive jet production cross section, for multiple Q^2 intervals (columns) as a function of the jet observables (rows) reported in this work. Predictions from multiple simulations are shown for comparison. The percent difference between data and predictions is shown in the bottom panels, split into dedicated DIS simulators (middle) and general purpose simulators (bottom). Gray bands represent the total systematic uncertainty. Statistical uncertainties for data events are shown as vertical bars, while statistical uncertainties from simulations are smaller than the marker size.

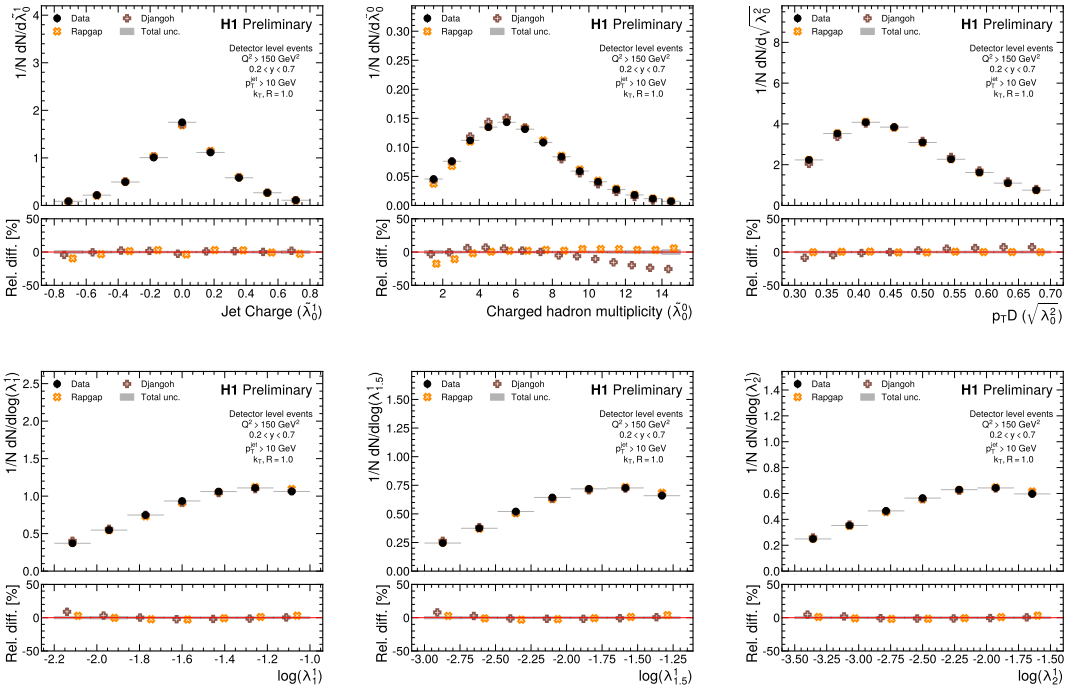

Fig. 4: Normalized number of jets at reconstruction level, as a function of the jet observables reported in this work. Predictions from DJANGOH and RAPGAP simulations are shown for comparison. The percent difference between data and predictions is shown in the bottom panel. Gray bands represent the total systematic uncertainty from detector effects. Statistical uncertainties for data events are shown as vertical bars, while statistical uncertainties from simulations are smaller than the marker size.

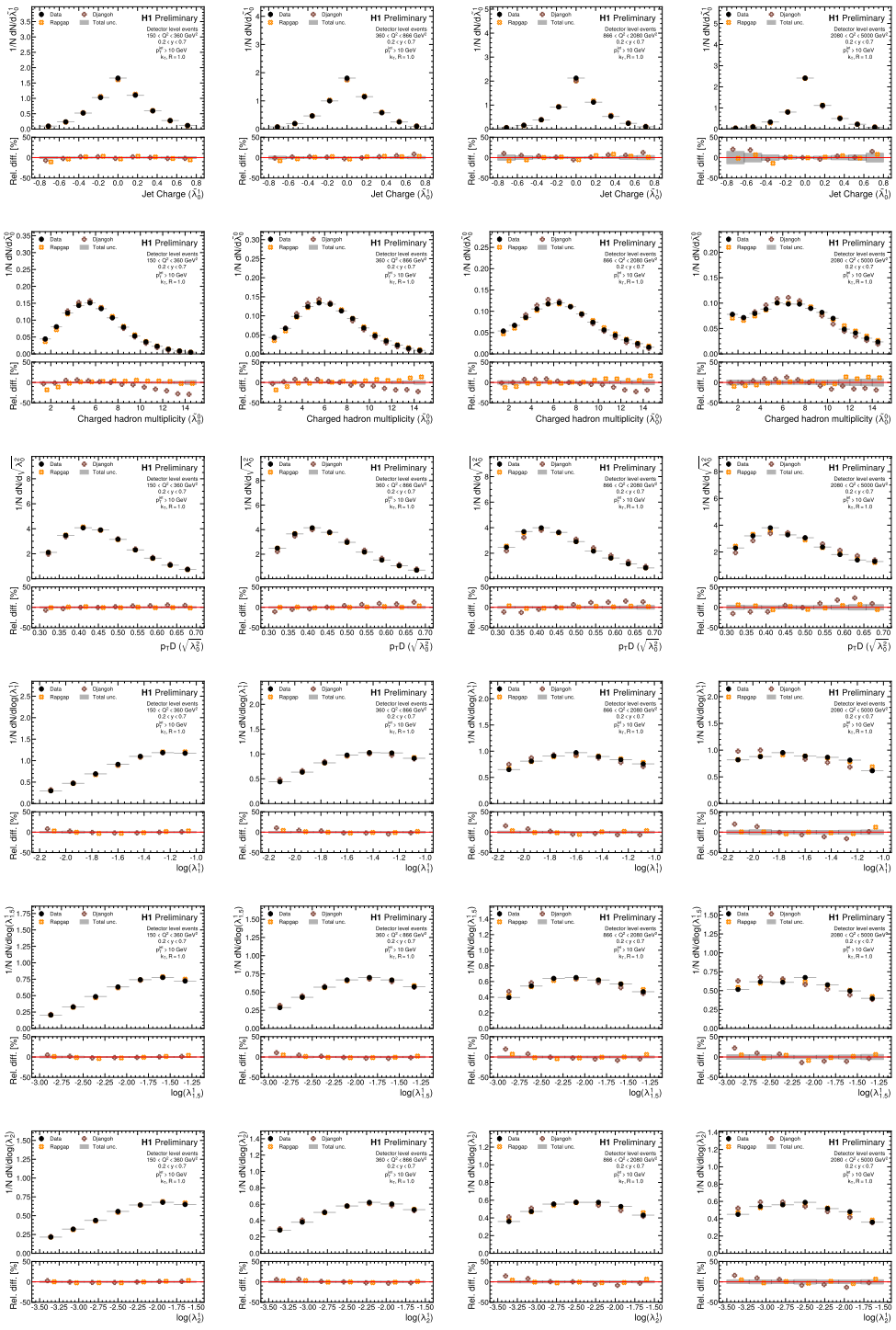

Fig. 5: Normalized number of jets at reconstruction level, for multiple Q^2 intervals (columns) as a function of the jet observables (rows) reported in this work. Predictions from DJANGOH and RAPGAP simulations are shown for comparison. The percent difference between data and predictions is shown in the bottom panel. Gray bands represent the total systematic uncertainty from detector effects. Statistical uncertainties for data events are shown as vertical bars, while statistical uncertainties from simulations are smaller than the marker size.

Bibliography

[1] ZEUS, J. Breitweg *et al.*, Eur. Phys. J. C **8**, 367 (1999), hep-ex/9804001.

[2] ZEUS, S. Chekanov *et al.*, Phys. Lett. B **558**, 41 (2003), hep-ex/0212030.

[3] ZEUS, S. Chekanov *et al.*, Nucl. Phys. B **700**, 3 (2004), hep-ex/0405065.

[4] H1, C. Adloff *et al.*, Nucl. Phys. B **545**, 3 (1999), hep-ex/9901010.

[5] A. J. Larkoski, J. Thaler, and W. J. Waalewijn, JHEP **11**, 129 (2014), 1408.3122.

[6] P. Gras *et al.*, JHEP **07**, 091 (2017), 1704.03878.

[7] D. Krohn, M. D. Schwartz, T. Lin, and W. J. Waalewijn, Phys. Rev. Lett. **110**, 212001 (2013), 1209.2421.

[8] CMS, S. Chatrchyan *et al.*, JHEP **04**, 036 (2012), 1202.1416.

[9] F. Pandolfi, *Search for the Standard Model Higgs Boson in the $H \to ZZ \to l^+l^-q\bar{q}$ Decay Channel at CMS*, PhD thesis, Zurich, ETH, New York, 2012.

[10] CMS, S. Chatrchyan *et al.*, (2013).

[11] R. D. Field and R. P. Feynman, Nucl. Phys. B **136**, 1 (1978).

[12] E. Farhi, Phys. Rev. Lett. **39**, 1587 (1977).

[13] S. Catani, G. Turnock, and B. R. Webber, Phys. Lett. B **295**, 269 (1992).

[14] P. E. L. Rakow and B. R. Webber, Nucl. Phys. B **191**, 63 (1981).

[15] R. K. Ellis and B. R. Webber, Conf. Proc. C **860623**, 74 (1986).

[16] E.-C. Aschenauer, K. Lee, B. S. Page, and F. Ringer, Phys. Rev. D **101**, 054028 (2020), 1910.11460.

[17] Z.-B. Kang, X. Liu, S. Mantry, and D. Y. Shao, Phys. Rev. Lett. **125**, 242003 (2020).

[18] H1, I. Abt *et al.*, (1993).

[19] H1 Calorimeter Group, B. Andrieu *et al.*, Nucl. Instrum. Meth. A **336**, 460 (1993).

[20] H1, I. Abt *et al.*, Nucl. Instrum. Meth. A **386**, 310 (1997).

[21] H1, I. Abt *et al.*, Nucl. Instrum. Meth. A **386**, 348 (1997).

[22] H1 SPACAL Group, R. D. Appuhn *et al.*, Nucl. Instrum. Meth. A **386**, 397 (1997).

[23] D. Pitzl *et al.*, Nucl. Instrum. Meth. A **454**, 334 (2000), hep-ex/0002044.

[24] H1 Calorimeter Group, B. Andrieu *et al.*, Nucl. Instrum. Meth. A **350**, 57 (1994).

[25] H1 Calorimeter Group, B. Andrieu *et al.*, Nucl. Instrum. Meth. A **336**, 499 (1993).

[26] H1, F. D. Aaron *et al.*, Eur. Phys. J. C **72**, 2163 (2012), 1205.2448, [Erratum: Eur.Phys.J.C 74, 2733 (2014)].

[27] H1, C. Adloff *et al.*, Eur. Phys. J. C **30**, 1 (2003), hep-ex/0304003.

[28] H1, F. D. Aaron *et al.*, JHEP **09**, 061 (2012), 1206.7007.

[29] H1, V. Andreev *et al.*, Eur. Phys. J. C **75**, 65 (2015), 1406.4709.

[30] H1, V. Andreev *et al.*, Eur. Phys. J. C **77**, 215 (2017), 1611.03421, [Erratum: Eur.Phys.J.C 81, 739 (2021)].

[31] U. Bassler and G. Bernardi, Nucl. Instrum. Meth. A **361**, 197 (1995), hep-ex/9412004.

[32] M. Peez, Search for deviations from the standard model in high transverse energy processes at the electron proton collider HERA, Other thesis, 2003.

[33] S. Hellwig, Untersuchung der $D^* - \pi_{slow}$ Double Tagging Methode in Charmanalysen, Master's thesis, Hamburg U., 2004.

[34] B. Portheault, First measurement of charged and neutral current cross sections with the polarized positron beam at HERA II and QCD-electroweak analyses, Other thesis, 2005.

[35] M. Cacciari, G. P. Salam, and G. Soyez, Eur. Phys. J. C **72**, 1896 (2012), 1111.6097.

[36] M. Cacciari and G. P. Salam, Phys. Lett. B **641**, 57 (2006), hep-ph/0512210.

[37] S. Catani, Y. L. Dokshitzer, M. H. Seymour, and B. R. Webber, Nucl. Phys. B **406**, 187 (1993).

[38] S. D. Ellis and D. E. Soper, Phys. Rev. D **48**, 3160 (1993), hep-ph/9305266.

[39] K. Charchula, G. A. Schuler, and H. Spiesberger, Comput. Phys. Commun. **81**, 381 (1994).

[40] H. Jung, Comput. Phys. Commun. **86**, 147 (1995).

[41] H. Spiesberger *et al.*, Radiative corrections at HERA, in *Workshop on Physics at HERA*, 1992.

[42] A. Kwiatkowski, H. Spiesberger, and H. J. Mohring, Z. Phys. C **50**, 165 (1991).

[43] A. Kwiatkowski, H. Spiesberger, and H. J. Mohring, Comput. Phys. Commun. **69**, 155 (1992).

[44] J. Pumplin *et al.*, JHEP **07**, 012 (2002), hep-ph/0201195.

[45] B. Andersson, G. Gustafson, G. Ingelman, and T. Sjostrand, Phys. Rept. **97**, 31 (1983).

[46] ALEPH, S. Schael *et al.*, Phys. Lett. B **606**, 265 (2005).

[47] L. Lonnblad, Comput. Phys. Commun. **71**, 15 (1992).

[48] R. Brun, F. Bruyant, M. Maire, A. C. McPherson, and P. Zanarini, (1987).

[49] T. Sjostrand, S. Mrenna, and P. Z. Skands, JHEP **05**, 026 (2006), hep-ph/0603175.

[50] T. Sjöstrand *et al.*, Comput. Phys. Commun. **191**, 159 (2015), 1410.3012.

[51] W. T. Giele, D. A. Kosower, and P. Z. Skands, Phys. Rev. D **78**, 014026 (2008), 0707.3652.

[52] W. T. Giele *et al.*, PoS **DIS2013**, 165 (2013), 1307.1060.

[53] S. Höche and S. Prestel, Eur. Phys. J. C **75**, 461 (2015), 1506.05057.

[54] NNPDF, R. D. Ball *et al.*, Eur. Phys. J. C **77**, 663 (2017), 1706.00428.

[55] L. A. Harland-Lang, A. D. Martin, P. Motylinski, and R. S. Thorne, Eur. Phys. J. C **75**, 204 (2015), 1412.3989.

[56] J. Bellm *et al.*, Eur. Phys. J. C **76**, 196 (2016), 1512.01178.

[57] M. Bahr *et al.*, Eur. Phys. J. C **58**, 639 (2008), 0803.0883.

[58] S. Dulat *et al.*, Phys. Rev. D **93**, 033006 (2016), 1506.07443.

[59] A. Andreassen, P. T. Komiske, E. M. Metodiev, B. Nachman, and J. Thaler, Phys. Rev. Lett. **124**, 182001 (2020), 1911.09107.

[60] A. Andreassen *et al.*, Scaffolding Simulations with Deep Learning for High-dimensional Deconvolution, in *9th International Conference on Learning Representations*, 2021, 2105.04448.

[61] L. B. Lucy, Astron. J. **79**, 745 (1974).

[62] W. H. Richardson, Journal of the Optical Society of America (1917-1983) **62**, 55 (1972).

[63] G. D'Agostini, Nucl. Instrum. Meth. A **362**, 487 (1995).

[64] P. T. Komiske, E. M. Metodiev, and J. Thaler, JHEP **01**, 121 (2019), 1810.05165.

[65] H. Qu and L. Gouskos, Phys. Rev. D **101**, 056019 (2020), 1902.08570.

[66] E. A. Moreno *et al.*, Eur. Phys. J. C **80**, 58 (2020), 1908.05318.

[67] E. A. Moreno *et al.*, Phys. Rev. D **102**, 012010 (2020), 1909.12285.

[68] V. Mikuni and F. Canelli, Eur. Phys. J. Plus **135**, 463 (2020), 2001.05311.

[69] E. Bernreuther, T. Finke, F. Kahlhoefer, M. Krämer, and A. Mück, SciPost Phys. **10**, 046 (2021), 2006.08639.

[70] J. Guo, J. Li, T. Li, and R. Zhang, Phys. Rev. D **103**, 116025 (2021), 2010.05464.

[71] M. J. Dolan and A. Ore, Phys. Rev. D **103**, 074022 (2021), 2012.00964.

[72] V. Mikuni and F. Canelli, Mach. Learn. Sci. Tech. **2**, 035027 (2021), 2102.05073.

[73] P. Konar, V. S. Ngairangbam, and M. Spannowsky, (2021), 2109.14636.

[74] C. Shimmin, (2021), 2107.02908.

[75] S. Gong *et al.*, (2022), 2201.08187.

[76] F. Chollet, Keras, https://github.com/fchollet/keras, 2017.

[77] M. Abadi *et al.*, Tensorflow: A system for large-scale machine learning., in *OSDI* Vol. 16, pp. 265–283, 2016.

[78] D. Kingma and J. Ba, (2014), 1412.6980.

[79] Perlmutter system, https://docs.nersc.gov/systems/perlmutter/system_details/, Accessed: 2022-05-04.

[80] A. Sergeev and M. D. Balso, arXiv preprint arXiv:1802.05799 (2018).

[81] R. Kogler, Measurement of jet production in deep-inelastic ep scattering at hera, 2011.

[82] H1, V. Andreev *et al.*, Eur. Phys. J. C **75**, 65 (2015), 1406.4709.

[83] H1, F. D. Aaron *et al.*, Eur. Phys. J. C **71**, 1769 (2011), 1106.1028, [Erratum: Eur.Phys.J.C 72, 2252 (2012)].

[84] H1, F. D. Aaron *et al.*, JHEP **09**, 061 (2012), 1206.7007.

[85] B. Efron, Annals Statist. **7**, 1 (1979).